


Regulating lithium affinity of hosts for reversible lithium metal batteries

Hao Liu¹ | Yuchen Ji¹ | Yang Li² | Shisheng Zheng^{1,3} | Zihang Dong⁴ | Kai Yang⁵ | Aimin Cao¹ | Yuxiang Huang¹ | Yinchao Wang¹ | Haifeng Shen⁶ | Shao-jian Zhang⁶ | Feng Pan¹ | Luyi Yang¹ 

¹School of Advanced Materials, Peking University Shenzhen Graduate School, Shenzhen, Guangdong, China

²Institute of Process Equipment, College of Energy Engineering, Zhejiang University, Hangzhou, Zhejiang, China

³College of Energy, Xiamen University, Xiamen, Fujian, China

⁴School of Environment and Energy, Peking University Shenzhen Graduate School, Shenzhen, Guangdong, China

⁵Advanced Technology Institute, Department of Electrical and Electronic Engineering, University of Surrey, Guildford, Surrey, UK

⁶School of Chemical Engineering, The University of Adelaide, Adelaide, South Australia, Australia

Correspondence

Yang Li, Institute of Process Equipment, College of Energy Engineering, Zhejiang University, Hangzhou, Zhejiang 310027, China.

Email: ly21@zju.edu.cn

Feng Pan and Luyi Yang, School of Advanced Materials, Peking University Shenzhen Graduate School, Shenzhen 518055, China.

Email: panfeng@pkusz.edu.cn and yangly@pkusz.edu.cn

Funding information

Science, Technology and Innovation Commission of Shenzhen Municipality, Grant/Award Number: JCYJ20200109140416788; Guangdong Provincial Department of Science and Technology, Grant/Award Number: 2017B030301013

Abstract

Lithium (Li) metal batteries are regarded as the “holy grail” of next-generation rechargeable batteries, but the poor redox reversibility of Li anode hinders its practical applications. While extensive studies have been carried out to design lithiophilic substrates for facile Li plating, their effects on Li stripping are often neglected. In this study, by homogeneously loading indium (In) single atoms on N-doped graphene via In-N bonds, the affinity between Li and hosting substrates is regulated. In situ observation of Li deposition/stripping processes shows that compared with the N-doped graphene substrate, the introduction of In effectively promotes its reversibility of Li redox, achieving a dendrite-free Li anode with much-improved coulombic efficiency. Interestingly, theoretical calculations demonstrate that In atoms have actually made the substrate less lithophilic via passivating the N sites to avoid the formation of irreversible Li–N bonding. Therefore, a “volcano curve” for reversible Li redox processes is proposed: the affinity of substrates toward Li should be optimized to a moderate value, where the balance for both Li plating and Li stripping processes could be reached. By demonstrating a crucial design principle for Li metal hosting substrates, our finding could trigger the rapid development of related research.

Hao Liu and Yuchen Ji authors contributed equally to this study.

This is an open access article under the terms of the [Creative Commons Attribution](https://creativecommons.org/licenses/by/4.0/) License, which permits use, distribution and reproduction in any medium, provided the original work is properly cited.

© 2024 The Authors. *Interdisciplinary Materials* published by Wuhan University of Technology and John Wiley & Sons Australia, Ltd.

KEYWORDS

in situ AFM, Li metal anode, lithiophilic sites, single atoms, volcano plot

1 | INTRODUCTION

The ever-increasing requirements for high energy density batteries urge researchers to develop energy storage systems beyond traditional Li-ion batteries. Therefore, electrode materials with higher theoretical capacity are proposed to replace the commercially used ones.^[1–5] Among various candidates, Li metal is regarded as the most promising alternative to traditional graphite anode because of its ultrahigh capacity and low redox potential of -3.04 V (vs. standard hydrogen electrode).^[6–8] Especially, when combined with sulfur^[9] or oxygen-based^[10] cathode, the energy density of full Li metal batteries could theoretically reach 650 and 950 Wh kg⁻¹, respectively.^[11–13] However, the practical application of Li has been long impeded by dendrite growth, which could potentially trigger a series of undesirable effects on batteries, including electrolyte consumption, accumulation of dead Li, and short-circuit of batteries. Generally, it is believed that the formation of the dendrite results from uneven nucleation and subsequent nonuniform deposition.^[14–16] Numerous efforts based on electrolyte optimization,^[17,18] artificial solid-state interface (SEI),^[19–21] and regulation of Li deposition^[22,23] have been demonstrated to suppress or eliminate dendrite growth.

Compared with approaches that form a thin passivating/protective layer to suppress dendrite growth, which might eventually fail after prolonged cycles,^[24,25] the regulation of Li deposition is considered a more effective way to achieve a dendrite-free Li anode via directing the Li deposition and homogenizing Li-ion flux on the electrode surface. Recently, Ag, Au, and some other noble metal-based nanoparticles have been employed as lithiophilic sites for homogeneous Li deposition.^[11,26] According to the characters of Li⁺ nucleation and deposition, smaller nucleation sites would be more advantageous for uniform Li⁺ deposition. In this way, lithiophilic metal atoms with isolated spatial distribution will be ideal for Li⁺ deposition. Besides, compared with nanoparticles, single atoms have higher electrochemical activity as well as complete atomic utilization.^[27,28]

Referring to the “volcano plot” in the catalysis process,^[29] it should be noted that reversible Li redox requires not only lithiophilic sites but also a desirable energy barrier for facile Li stripping.^[30–32] Therefore, to realize both homogeneous Li plating and reversible Li stripping, the affinity between the hosting substrate and

lithium should be optimized. Zhang et al. previously applied the nitrogen-doped carbon (NC) as the Li plating matrix to regulate Li metal nucleation and suppress dendrite growth.^[22] Herein, we introduce the single atom dispersion of indium (In) on NC substrates (SAIn-NC) to further optimize Li deposition and stripping behaviors. By combining in situ atomic force microscope (AFM) observation with density functional theory (DFT) calculation, the mechanism of reversible Li redox is revealed. Although the high binding energy of nitrogen-doped graphene with Li atoms is conducive to homogeneous Li deposition, excessive binding energy will impede the stripping process with the formation of Li–N bonds, which is detrimental to reversibility. By introducing single atoms dispersed on the graphene substrate, the binding energy is adjusted to a moderate level, balancing both the deposition and stripping processes. Owing to the optimized Li stripping pathway, improved average coulombic efficiency can be achieved in Li||Cu cells. Through shedding light on some key aspects of reversible Li plating and stripping, this work will be of guiding significance in substrate design for Li metal anodes.

2 | RESULTS AND DISCUSSIONS

SAIn-NC was synthesized via the pyrolysis of dicyan diamide (DCDA), glucose (GC), and In(III) chloride (InCl₃) under the Ar atmosphere (Figure 1A). NC was obtained through a similar method in the absence of InCl₃. As shown in Figure 1B, there is no distinct difference in X-ray powder diffraction patterns between SAIn-NC and NC, indicating that both the substrates are amorphous structures and the In element is non-crystalline. The peak at 43.25° can be attributed to the (100) of graphene.^[33,34] This result is further confirmed by the TEM images (Supporting Information S1: Figure S1) of SAIn-NC, where no obvious In cluster can be observed. The atomic ratios of In and N are about 0.14 and 20.96 at%, respectively (Supporting Information S1: Figure S2). The chemical state of the In element in SAIn-NC can be verified by X-ray photoelectron spectroscopy (XPS). As presented in Figure 1C, the In 3d_{5/2} peak is at 444.7 eV, located between the In⁰ (443.08 eV) and In³⁺ (445.7 eV), indicating the existence of the In–N bond located at about 445 eV.^[35] According to the scanning transmission electron microscopy (STEM) image and the corresponding energy dispersive

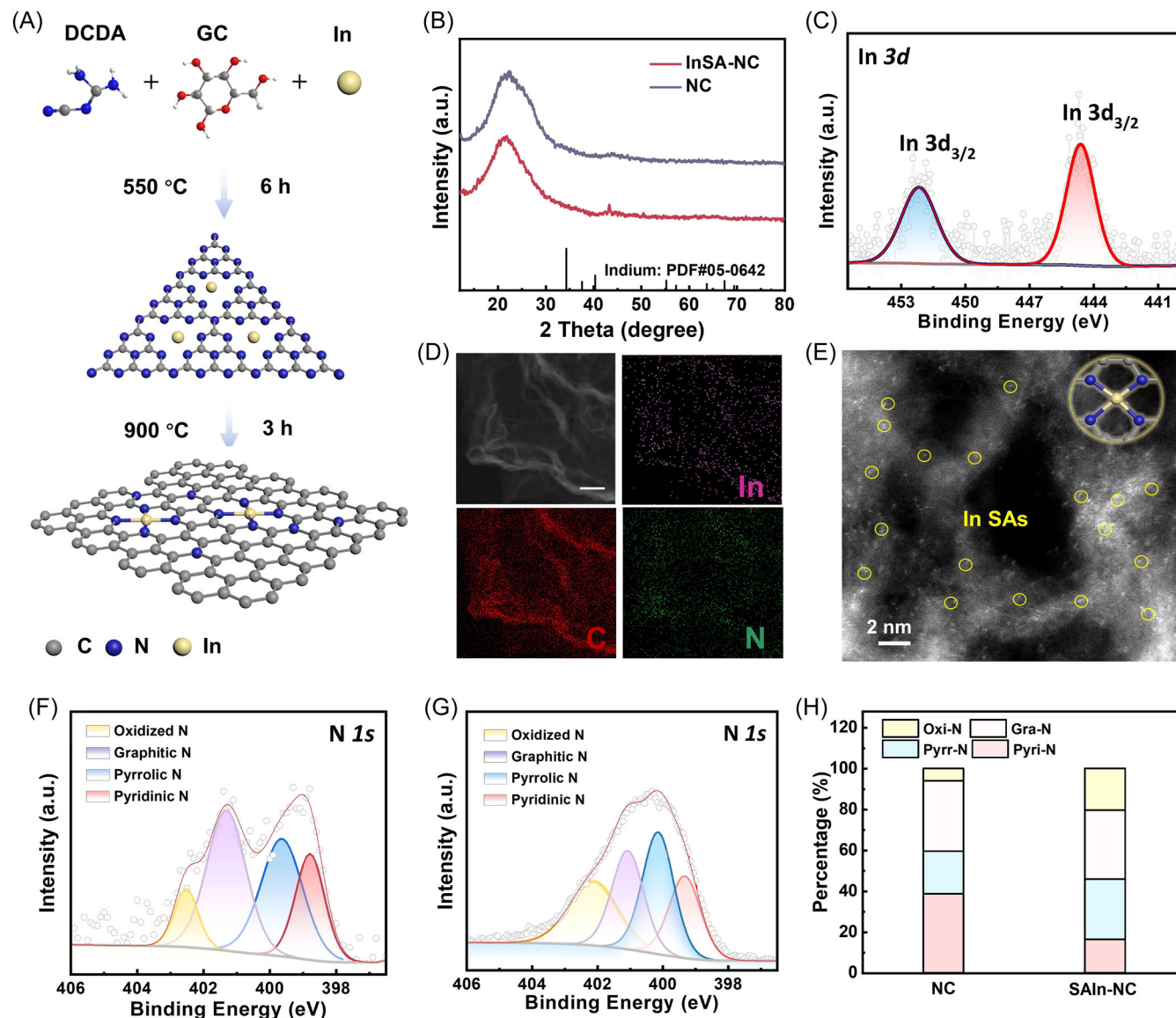


FIGURE 1 Material fabrication and characterizations. (A) Schematic of the single atom dispersion of indium (In) on nitrogen-doped carbon (SAIn-NC) synthesis process. (B) X-ray diffraction results of the SAIn-NC (red) and NC (blue). (C) X-ray photoelectron spectroscopy (XPS) of In 3d for SAIn-NC. (D) Elemental mapping of In, C, and N based on the scanning transmission electron microscopy (STEM) image (scale bar: 20 nm). (E) High-angle annular dark-field-STEM images of the SAIn-NC. (F, G) XPS of N 1s for NC (F) and SAIn-NC (G). (H) The percentage of various N species in NC and SAIn-NC, respectively, obtained according to XPS results. DCDA, cyanoguanidine; GC, glucose.

spectra (Figure 1D), the synthesized SAIn-NC exhibits a graphene-like structure evenly dispersed with In, N, O, and C elements, directly revealing the uniform distribution of In atom in the NC matrix without nanoparticle or large cluster. Furthermore, the position of In atoms of SAIn-NC are also identified via high-angle annular dark-field scanning transmission electron microscopy (Figure 1E and Supporting Information S1: Figure S3), where the brighter spots represent heavier atoms (i.e., In for this study). In atoms are well dispersed and evenly distributed within the graphene substrate, further confirming their monodispersion.

In the Raman spectra of both NC-based substrates (Supporting Information S1: Figure S5), a new peak was detected at around 1140 cm^{-1} in SAIn-NC, which can be attributed to the introduction of In atoms to the substrate forming the In–N bonds, proved via theoretical calculation (Supporting Information S1: Figure S6). The N 1s XPS spectra of both substrates (Figure 1F,G) exhibited the coexistence of four types of nitrogen species, including oxidized nitrogen (402.25 eV), graphitic nitrogen (401.3 eV), pyrrolic nitrogen (400.05 eV), and pyridinic nitrogen (399.7 eV).^[36] Interestingly, the introduction of SAIn into the NC also modified the ratios of various N species by

lowering the ratio of pyridinic nitrogen, with the increase of pyrrolic nitrogen and oxidized nitrogen (Figure 1H).

Next, in situ AFM^[37] was applied for real-time observation of the nucleation as well as the subsequent Li deposition and stripping on bare Cu, NC, and SAIn-NC substrates. The setup shows (Supporting Information S1: Figure S7) that Cu is sputtered on the surface of the ultrasmooth silicon wafer to simulate the Cu current collector. NC and SAIn-NC materials are coated on the Cu-coated silicon wafer to serve as a working electrode, and a lithium ring serves as the counter and reference electrode. For the pristine Cu substrate, a flat and smooth surface at open-circuit potential (OCP) can be observed (Figure 2A). Upon applying a constant reduction current, Li deposition begins and scattered Li nucleation sites can be observed when discharging time reaches 15 min (Figure 2B). With more Li metal getting continuously deposited at the previous nucleation sites, they grow into much larger aggregates (Figure 2C). The ex situ SEM image (Supporting Information S1: Figure S8a) also confirms large

toroid-shaped Li deposition on Cu. Moreover, the highly clustered Li metal with random distribution exhibits poor reversibility (Figure 2D,E); after the same amount of charging time, the main bulk of Li metal still remained on the Cu substrate, indicating low coulombic efficiency, which coincided with the SEM image (Supporting Information S1: Figure S9).

In comparison, the Li redox behaviors are much different on NC- and SAIn-NC-coated Cu current collectors. As presented in Figure 2F,K, graphene nanosheets with diameters ~100 nm are evenly distributed on Cu at OCP. As the deposition process begins, Li metal is homogeneously nucleated on the graphene nanosheets (Figure 2G,L), rather than arbitrarily depositing on bare Cu substrate. By comparing the deposition morphology after 30 min, SAIn-NC (Figure 2M) exhibits more homogeneous Li deposition than NC (Figure 2H). This in situ observed difference is supported by the ex situ SEM images (Supporting Information S1: Figure S8b,c), where Li deposited on SAIn-NC is much more compact than that on NC despite the similar crystalline sizes.

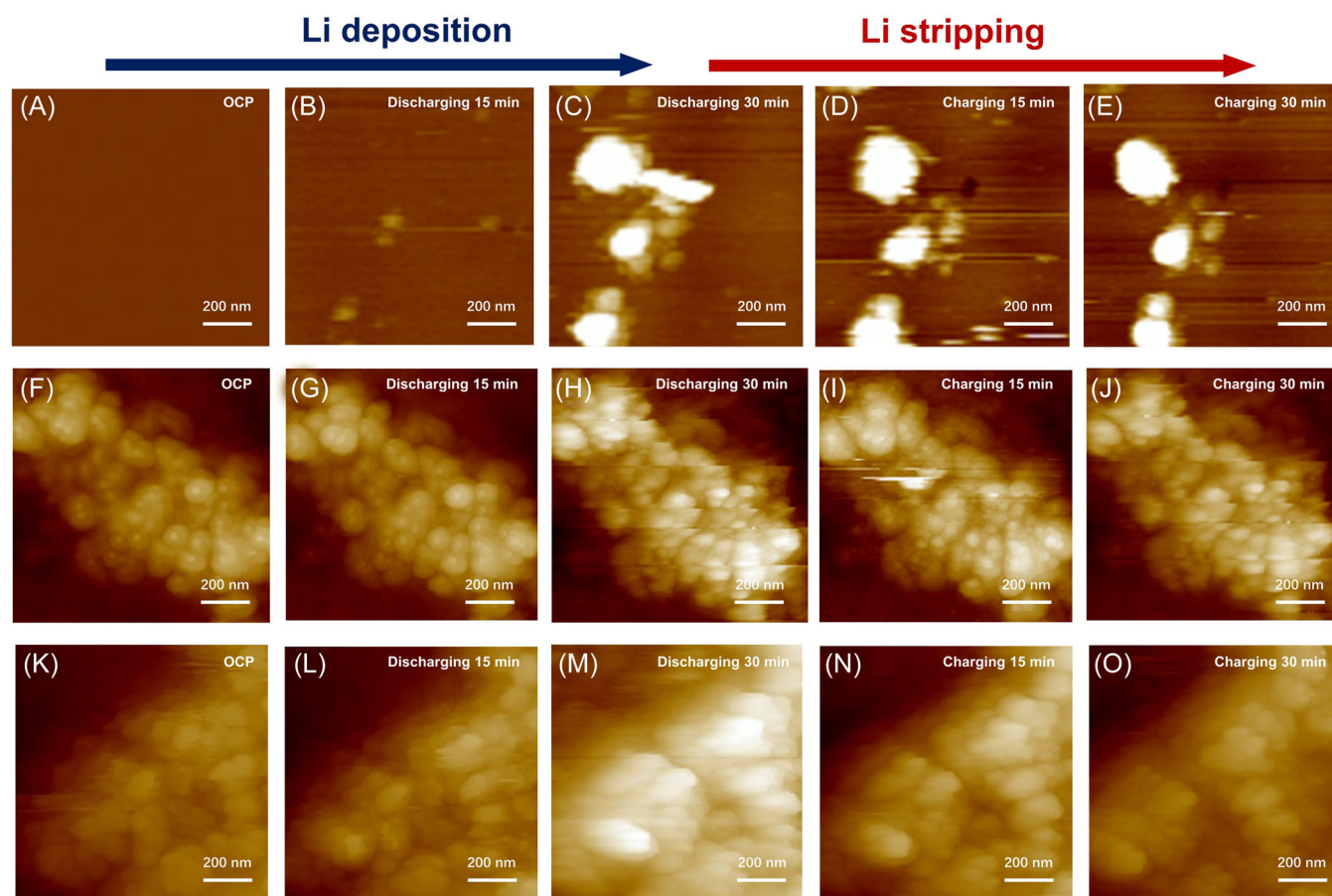


FIGURE 2 In situ AFM observation of lithium deposition and stripping processes at different discharging and charging times on bare (A–E) Cu, (F–J) nitrogen-doped carbon (NC), and (K–O) single atom dispersion of indium-NC (SAIn-NC). A constant current density of 0.05 mA cm^{-2} was applied for all tests. AFM, atomic force microscope; OCP, open-circuit potential.

Moreover, SAIn-NC also exhibits higher Li stripping reversibility than NC. Upon oxidation, deposited Li metal gradually stripped away from NC, as shown in Figure 2I. However, after 30 min, there is still a small part of the deposited Li metal that remains on the substrate (Figure 2J), demonstrating a distinctly different morphology compared with pristine NC (Figure 2F) and suggesting a compromised coulombic efficiency. By contrast, a more rapid response of Li stripping can be observed on SAIn-NC (Figure 2N). After 30 min of charging, a fresh graphene surface can be obtained (Figure 2O), which exhibits a similar morphology to the pristine SAIn-NC (Figure 2K), indicating a drastically enhanced Li stripping reversibility.

The regulation of Li deposition with enhanced reversibility plays an important role in the performance of Li anodes. To further evaluate the long-term reversibility and dendrite-inhibiting ability of SAIn, half cells with different working electrodes (Cu, NC, and SAIn-NC) and Li counter electrodes were assembled and tested. As is shown in Figure 3A, the SAIn-NC anode shows stable coulombic efficiency as high as 97.66% at the current density of 1 mA cm^{-2} areal capacity $^{-1}$ of 1 mAh cm^{-2} after operating for 500 cycles. By contrast, the coulombic efficiency of the NC anode begins to fluctuate after 150 cycles, followed by a rapid decrease to 70%. As for the bare Cu anode, the coulombic efficiency declines sharply at only 60 cycles. When the content of In further increased, the In-based cluster formed. The agglomerated In nanoparticle is unfavorable for homogeneous Li deposition and results in the attenuation of electrochemical performance (Supporting Information S1: Figure S10). Under an elevated current density (2 mA cm^{-2}) and areal capacity (2 mAh cm^{-2}), respectively, the coulombic efficiency of SAIn-NC anode remains over 98% after 100 cycles (Figure 3B), which outperforms both NC anode (44% over 70 cycles) and bare Cu anode (7% over 50 cycles). Combining the cycling results with in situ AFM results, it is rational to speculate that the drastic contrast in cycling performance is attributed to the different Li deposition and stripping behaviors. The voltage profiles of half cells with different substrates are presented in Figure 3C. The magnified voltage profile clearly shows that during the Li deposition process, the voltage hysteresis for SAIn-NC (15 mV) and NC (17 mV) is much lower than that of Cu (26 mV) at the current density of 1 mA cm^{-2} . The low Li plating overpotential on NC-based anodes indicates the formation of a stable and uniform interface, thus reducing the mass-transfer-controlled overpotential. During Li stripping, SAIn-NC delivers a lower overpotential (14 mV) compared with NC (20 mV) and bare Cu (30 mV). The above results are in good accordance with in situ AFM

results that SAIn-NC exhibits the highest reversibility. In addition, as shown in Figure 3D, during the long cycling in SAIn-NC, both depositing and stripping potentials remain unchanged for 300 cycles with fluctuations less than 5 mV, exhibiting high interfacial stability. However, based on the initial depositing and stripping curves of the three substrates (Supporting Information S1: Figure S11), due to the increased specific surface area in contact with the electrolytes, NC exhibits lower reversibility than Cu in the initial cycles. This can be attributed to additional side reactions involving the decomposition of electrolytes before the deposition of Li metal (above 0 V).^[38] Furthermore, the coulombic efficiency becomes even lower upon introducing In into NC, suggesting that the single atoms of In may catalyze electrolyte side reactions during initial cycles. However, this catalysis can be inhibited after the stabilization of the SEI layer^[39,40] in subsequent cycles (Figure 3A,B). Thus, while SAIn-NC itself may not be suitable for assembling anode-free batteries, it holds significant potential for application as Li-hosting substrates through predeposition of a Li anode onto the substrate or introducing sacrificial prelithiating agents to the cathode.^[41]

To evaluate the practical application prospect of SAIn-NC, full cells were assembled using different substrates (with 2 mAh of electrochemically predeposited Li) as anodes and LiFePO_4 as the cathode material. The SAIn-NC-based anode delivers the highest capacity retention of 75% after 200 cycles, which is much higher than NC and bare Cu (37.5% and 18.8%) (Figure 3E). The electrochemical curves (Supporting Information S1: Figure S12) show that the SAIn-NC-based anode also delivers the lowest overpotential in full cells. The improved full-cell performance obtained from SAIn-NC is attributed to its higher average coulombic efficiency, which suppresses the consumption of active Li. Furthermore, benefiting from the lower depositing and stripping overpotential, SAIn-NC also exhibits drastically improved rate performance of LiFePO_4 full cells up to 5 C (Figure 3F).

The above results have demonstrated that, although both NC and the SAIn-NC could facilitate uniform Li nucleation during the Li deposition process, it is easier for Li to be stripped away from SAIn-NC than NC, hence the higher reversibility. To reveal the intrinsic mechanisms, we applied DFT calculations to simulate the interatomic interaction between Li and both substrates. As presented in Figure 4A,B, upon the introduction of In single atoms, the binding energies of Li with the pyridinic/pyrrolic-N decrease from $-5.28/-5.95$ to $-1.64/-2.55$ eV, respectively. According to previous studies, the main contributing factor of N-doped graphene to promoted Li deposition is the high binding

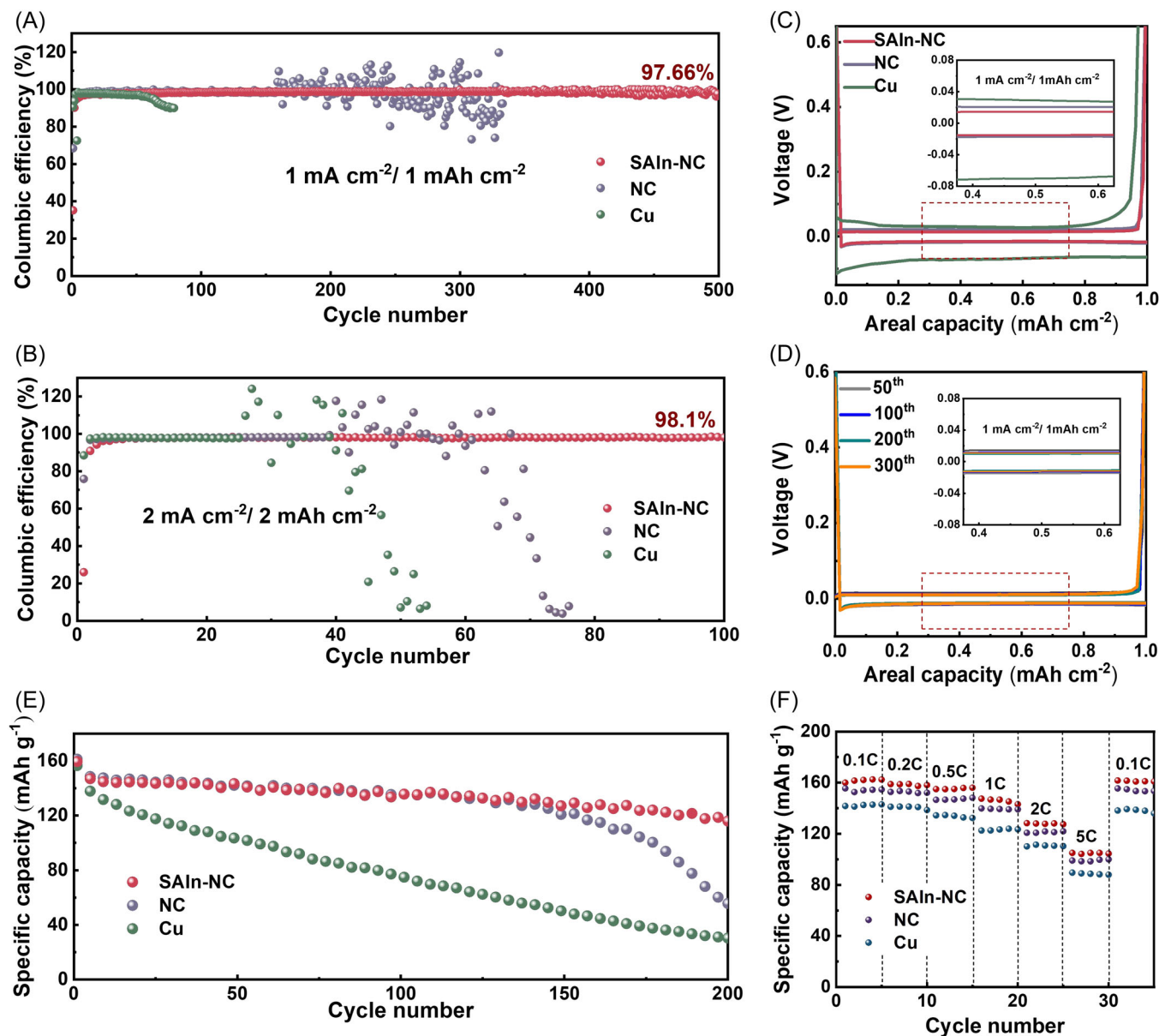


FIGURE 3 Electrochemical performances. (A) Coulombic efficiency of single atom dispersion of indium (In) on nitrogen-doped carbon (SAln-NC), NC, and Cu foil at the current density of 1 mA cm^{-2} , with the cycling capacity of 1 mAh cm^{-2} . (B) Coulombic efficiency of SAln-NC, NC, and Cu foil at the current density of 2 mA cm^{-2} , with the cycling capacity of 2 mAh cm^{-2} . (C) Voltage profiles of SAln-NC, NC, and Cu foil at the 30th cycle with a cycling capacity of 1 mAh cm^{-2} at 1 mA cm^{-2} . (D) Voltage profiles of the 50th, 100th, 200th, and 300th cycle of SAln-NC electrode with a cycling capacity of 1 mAh cm^{-2} at 1 mA cm^{-2} . (E) Cycling performance of LiFePO₄ full cells with SAln-NC, NC, and Cu foil. (F) Rate performance of LiFePO₄ full cells with SAln-NC, NC, and Cu foil.

energy between pyrrolic- or pyridinic-N species with Li atoms,^[42] which induces preferential Li nucleation on such lithiophilic sites. Therefore, the lowered binding energies in the presence of In should have resulted in inferior electrochemical performance compared with NC, whereas the experimental results suggest otherwise. We speculate that the excessive binding energy amplifies the uneven distribution of nitrogen in NC, causing the inhomogeneous deposition process of Li metal as presented in Figure 2F–O.

To illustrate the role of In atoms in the different Li deposition and stripping behaviors, the charge density difference of NC (Figure 4C) and SAln-NC (Figure 4D) is demonstrated, where the yellow and light blue surfaces correspond to the charge gain and lost regions, respectively. Through comparison, it is clear that the charge gain regions of Li with NC concentrate on the substrate, while the charge gain regions of Li with SAln-NC concentrate near In atoms. This result suggests that on NC, Li⁺ tends to bond with N and forms Li–N bonds on

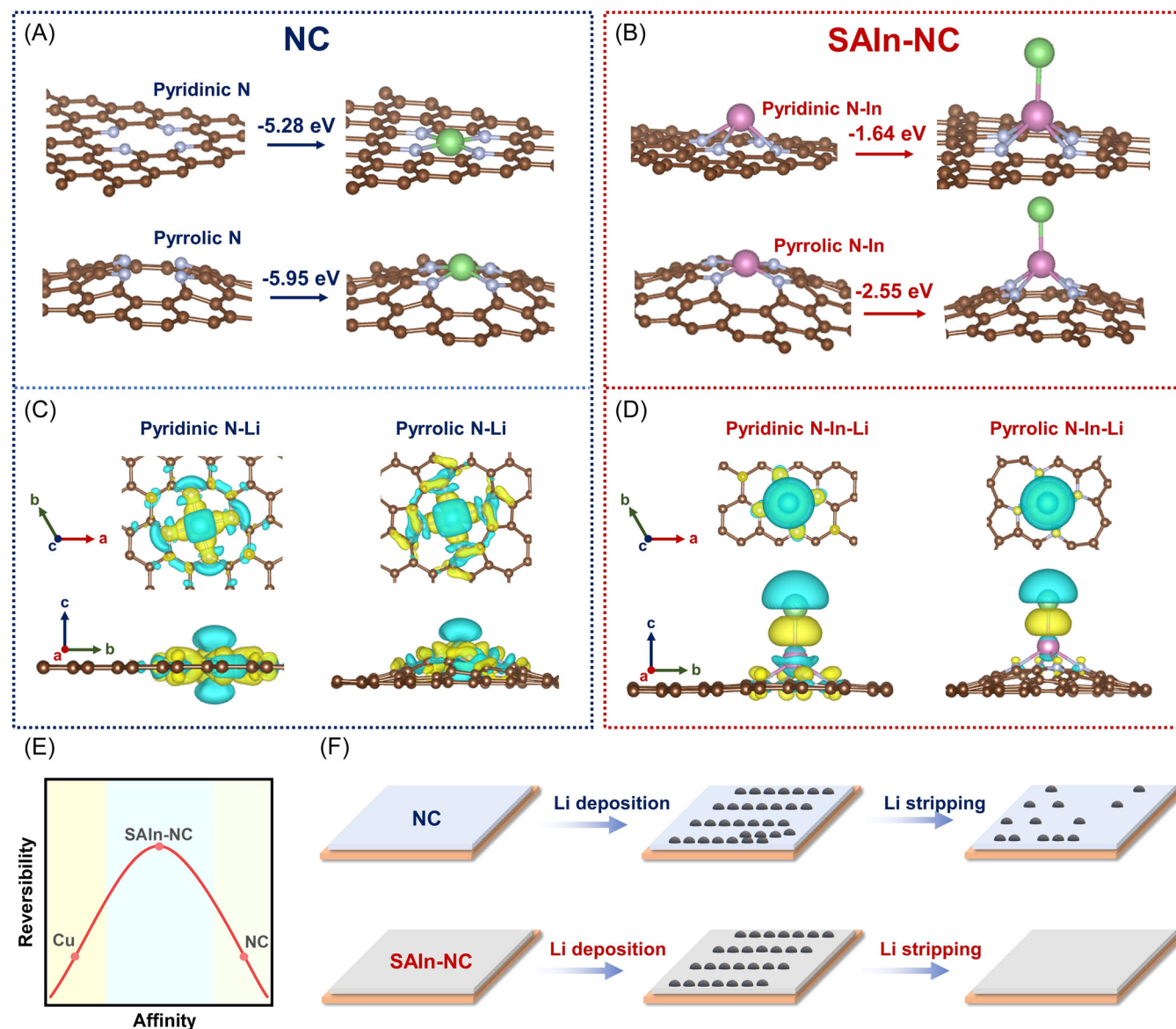


FIGURE 4 Binding energy of Li atom to the pyridinic-N and pyrrolic-N on N-doped graphene before (A) and after (B) doping with In single atom. Differential charge density of the most stable configurations adsorbed to the pyridinic-N and pyrrolic-N on N-doped graphene before (C) and after (D) doping with In single atom (isosurface value: $0.01 \text{ e } \text{\AA}^{-3}$). The Li, C, N, and In are marked with green, brown, silver, and purple, respectively. (E) The proposed “volcano curve” describes the Li affinity–reversibility correlation. (F) Schematic illustration of different Li depositing and stripping on different substrates.

NC, whereas on SAln-NC, through forming In–N bonds, the introduced In atoms “passivate” N atoms and become the deposition site for Li instead. To verify this speculation, Raman spectra of cycled NC and SAln-NC are compared (Supporting Information S1: Figure S13). The cycled NC electrode also exhibits a strong Raman peak of Li_3N ,^[43] which is much weaker on the cycled SAln-NC. Combining the Raman spectra with the theoretical calculation results, it can be concluded that the introduction of In single atoms effectively inhibits the formation of Li–N ionic bonds, which are difficult to

break during the Li stripping process. Instead, Li ions tend to form Li–In metallic bonds with In atoms, facilitating a more reversible stripping process. Owing to the single-atom distribution of the In element, the Li atom can only bond with the In single atom at the surface of NC, rather than forming a homogeneous alloy phase. Similar to “volcano curves” in heterogeneous catalysis^[29] (Figure 4E), the high binding energy between Li and the substrate is generally favorable for Li plating; however, as the binding energy becomes excessive, the energy barrier for Li desorption could be too high and Li

stripping process could become the rate-determining step for reversible Li redox, leading to unreacted Li on the substrate. Therefore, via introducing atomically dispersed In into NC, the binding energy is optimized to a moderate value, which is sufficient for facile and homogeneous Li deposition without impeding Li desorption. By balancing the reaction kinetics for both Li plating and stripping processes, reversible Li redox can be achieved (Figure 4F).

3 | CONCLUSIONS

In conclusion, the deposition and stripping behaviors of Li^+ on bare Cu, NC, and SAln-NC are systematically investigated via in situ AFM and theoretical calculations. Although increasing the binding energy of Li ions to the substrate can effectively regulate the deposition behavior, excessive value in N-doped graphene may also cause the formation of Li–N ionic bonds, which are too strong for reversible Li stripping. Herein, the affinity between Li- and N-doped graphene is regulated by uniformly loading indium single atoms to “passivate” N sites so that Li–In metallic bonds can be formed instead of Li–N ionic bonds, which facilitate the Li stripping process and drastically enhance the reversibility. Hence, we propose a “volcano curve” for reversible Li redox processes in which the affinity of substrates toward Li should be optimized to a moderate value to balance both Li plating and Li stripping processes. Such a principle can also provide a fresh perspective on the design and optimization of the matrix for other metal anodes beyond Li, including Na metal, K metal, Zn metal, and so forth.

ACKNOWLEDGMENTS

This work was supported by the Shenzhen Science and Technology Research grant (JCYJ20200109140416788) and the Soft Science Research Project of Guangdong Province (2017B030301013).

CONFLICT OF INTEREST STATEMENT

The authors declare no conflict of interest.

ORCID

Luyi Yang  <http://orcid.org/0000-0002-5516-9829>

REFERENCES

- [1] Wang Z, Sun Z, Li J, et al. Insights into the deposition chemistry of Li ions in nonaqueous electrolyte for stable Li anodes. *Chem Soc Rev*. 2021;50:3178–3210.
- [2] Gao Y, Yan Z, Gray JL, et al. Polymer–inorganic solid–electrolyte interphase for stable lithium metal batteries under lean electrolyte conditions. *Nat Mater*. 2019;18:384–389.
- [3] Liu J, Bao Z, Cui Y, et al. Pathways for practical high-energy long-cycling lithium metal batteries. *Nat Energy*. 2019;4:180–186.
- [4] Liu T, Wang J, Xu Y, Zhang Y, Wang Y. Dendrite-free and stable lithium metal battery achieved by a model of stepwise lithium deposition and stripping. *Nano Micro Lett*. 2021;13:170.
- [5] Huang W, Yang L, Chen Z, et al. Elastic lattice enabling reversible tetrahedral Li storage sites in a high-capacity manganese oxide cathode. *Adv Mater*. 2022;34:e2202745.
- [6] Fu J, Ji X, Chen J, et al. Lithium nitrate regulated sulfone electrolytes for lithium metal batteries. *Angew Chem Int Ed*. 2020;59:22194–22201.
- [7] Chen S, Niu C, Lee H, et al. Critical parameters for evaluating coin cells and pouch cells of rechargeable Li-metal batteries. *Joule*. 2019;3:1094–1105.
- [8] Xiang J, Yang L, Yuan L, et al. Alkali-metal anodes: from lab to market. *Joule*. 2019;3:2334–2363.
- [9] Ji Y, Yang K, Liu M, et al. PIM-1 as a multifunctional framework to enable high-performance solid-state lithium-sulfur batteries. *Adv Funct Mater*. 2021;31:2104830.
- [10] Wang XX, Guan DH, Li F, Li ML, Zheng LJ, Xu JJ. Magnetic and optical field multi-ssisted Li-O(2) batteries with ultrahigh energy efficiency and cycle stability. *Adv Mater*. 2022;34:e2104792.
- [11] Zheng G, Lee SW, Liang Z, et al. Interconnected hollow carbon nanospheres for stable lithium metal anodes. *Nat Nanotechnol*. 2014;9:618–623.
- [12] Jin C, Liu T, Sheng O, et al. Rejuvenating dead lithium supply in lithium metal anodes by iodine redox. *Nat Energy*. 2021;6:378–387.
- [13] Kim H, Choi W, Yoon J, et al. Exploring anomalous charge storage in anode materials for next-generation Li rechargeable batteries. *Chem Rev*. 2020;120:6934–6976.
- [14] Zhu M, Li B, Li S, Du Z, Gong Y, Yang S. Dendrite-free metallic lithium in lithiophilic carbonized metal-organic frameworks. *Adv Energy Mater*. 2018;8:1703505.
- [15] Yan K, Lu Z, Lee H-W, et al. Selective deposition and stable encapsulation of lithium through heterogeneous seeded growth. *Nat Energy*. 2016;1:16010.
- [16] Wang Y. Separator wettability enhanced by electrolyte additive to boost the electrochemical performance of lithium metal batteries. *Nano Micro Lett*. 2021;13:210.
- [17] Hu J, Ji Y, Zheng G, et al. Influence of electrolyte structural evolution on battery applications: cationic aggregation from dilute to high concentration. *Aggregate*. 2022;3:e153.
- [18] Shadike Z, Lee H, Borodin O, et al. Identification of LiH and nanocrystalline LiF in the solid-electrolyte interphase of lithium metal anodes. *Nat Nanotechnol*. 2021;16:549–554.
- [19] Gao S, Sun F, Liu N, Yang H, Cao P-F. Ionic conductive polymers as artificial solid electrolyte interphase films in Li metal batteries—a review. *Mater Today*. 2020;40:140–159.
- [20] Zou Y, Ma Z, Liu G, et al. Non-flammable electrolyte enables high-voltage and wide-temperature lithium-ion

- batteries with fast charging. *Angew Chem Int Ed.* 2023;135: e202216189.
- [21] Song H, Xue S, Chen S, et al. Polymeric wetting matrix for a stable interface between solidstate electrolytes and li metal anode. *Chin J Struct Chem.* 2022;41:2205048-2205054.
- [22] Zhang R, Chen XR, Chen X, et al. Lithiophilic sites in doped graphene guide uniform lithium nucleation for dendrite-free lithium metal anodes. *Angew Chem Int Ed.* 2017;56:7764-7768.
- [23] Yang Z, Dang Y, Zhai P, et al. Single-atom reversible lithiophilic sites toward stable lithium anodes. *Adv Energy Mater.* 2022;12:2103368.
- [24] Zhai P, Wang T, Jiang H, et al. 3D artificial solid-electrolyte interphase for lithium metal anodes enabled by insulator-metal-insulator layered heterostructures. *Adv Mater.* 2021; 33:e2006247.
- [25] Zhang S. Suppressing Li dendrites via electrolyte engineering by crown ethers for lithium metal batteries. *Nano Micro Lett.* 2020;12:158.
- [26] Yang C, Yao Y, He S, Xie H, Hitz E, Hu L. Ultrafine silver nanoparticles for seeded lithium deposition toward stable lithium metal anode. *Adv Mater.* 2017;29:1702714.
- [27] Li Y, Lin S, Wang D, et al. Single atom array mimic on ultrathin MOF nanosheets boosts the safety and life of lithium-sulfur batteries. *Adv Mater.* 2020;32:e1906722.
- [28] Liu F, Shi L, Lin X, et al. Fe/Co dual metal catalysts modulated by S-ligands for efficient acidic oxygen reduction in PEMFC. *Sci Adv.* 2023;9:eadg0366.
- [29] Wodrich MD, Sawatlon B, Busch M, Corminboeuf C. The genesis of molecular volcano plots. *Acc Chem Res.* 2021;54: 1107-1117.
- [30] Yang S, He R, Zhang Z, Cao Y, Gao X, Liu X. CHAIN: Cyber Hierarchy and Interactional Network Enabling Digital Solution for battery full-lifespan management. *Matter.* 2020;3:27-41.
- [31] Yu Y, Huang G, Wang JZ, Li K, Ma JL, Zhang XB. In situ designing a gradient Li(+) capture and quasi-spontaneous diffusion anode protection layer toward long-Life Li-O(2) batteries. *Adv Mater.* 2020;32:e2004157.
- [32] Heiskanen SK, Kim J, Lucht BL. Generation and evolution of the solid electrolyte interphase of lithium-ion batteries. *Joule.* 2019;3:2322-2333.
- [33] Cheng N, Wang H, Li X, Zhu L. Amperometric glucose biosensor based on integration of glucose oxidase with palladium nanoparticles/reduced graphene oxide nanocomposite. *Am J Anal Chem.* 2012;3:312-319.
- [34] Nazim S, Kousar T, Shahid M, et al. New graphene-Co_xZn_{1-x}Fe₂O₄ nano-heterostructures: magnetically separable visible light photocatalytic materials. *Ceram Int.* 2016;42: 7647-7654.
- [35] Lu P, Tan X, Zhao H, et al. Atomically dispersed indium sites for selective CO(2) electroreduction to formic acid. *ACS Nano.* 2021;15:5671-5678.
- [36] Shang H, Wang T, Pei J, et al. Design of a single-atom indium^{δ+}-N₄ interface for efficient electroreduction of CO₂ to formate. *Angew Chem Int Ed.* 2020;59:22465-22469.
- [37] Liu M, Yao L, Ji Y, et al. Nanoscale ultrafine zinc metal anodes for high stability aqueous zinc ion batteries. *Nano Lett.* 2023;23:541-549.
- [38] Ji Y, Qiu J, Zhao W, et al. In situ probing the origin of interfacial instability of Na metal anode. *Chem.* 2023;9:2943-2955.
- [39] Xiao P, Yun X, Chen Y, et al. Insights into the solvation chemistry in liquid electrolytes for lithium-based rechargeable batteries. *Chem Soc Rev.* 2023;52:5255-5316.
- [40] Wan H, Xu J, Wang C. Designing electrolytes and interphases for high-energy lithium batteries. *Nat Rev Chem.* 2023;8:30-44.
- [41] Qiao Y, Yang H, Chang Z, Deng H, Li X, Zhou H. A high-energy-density and long-life initial-anode-free lithium battery enabled by a Li₂O sacrificial agent. *Nat Energy.* 2021;6: 653-662.
- [42] Liu L, Yin YX, Li JY, Wang SH, Guo YG, Wan LJ. Uniform lithium nucleation/growth induced by lightweight nitrogen-doped graphitic carbon foams for high-performance lithium metal anodes. *Adv Mater.* 2018;30:1706216.
- [43] Chandrasekhar HR, Bhattacharya G, Migoni R, Bilz H. Infrared and Raman spectra and lattice dynamics of the superionic conductor Li₃N. *Phys Rev B.* 1978;17:884-893.

SUPPORTING INFORMATION

Additional supporting information can be found online in the Supporting Information section at the end of this article.

How to cite this article: Liu H, Ji Y, Li Y, et al. Regulating lithium affinity of hosts for reversible lithium metal batteries. *Interdiscip Mater.* 2024;3: 297-305. doi:10.1002/idm2.12153